Hopper flow of irregular shaped particles (non-convex polyhedra): GPU-based DEM simulation and experimental validation

Nicolin Govender[1,2], Daniel N. Wilke[3], Chuan-Yu Wu[1], Wenjie XU[5], Patrick Pizette[4],Johannes Khinast[2,6]

[1]Department of Chemical Engineering, University of Surrey, United Kingdom

[2]Research Center Pharmaceutical Engineering, GmbH, Graz, Austria

[3]Department of Mechanical and Aeronautical Engineering, University of Pretoria, South Africa

[4]Laboratoire Genie Civil et geo-Environnement, IMT Lille Douai, France

[5]Institute of Geotechnical Engineering, Department of Hydraulic Engineering Tsinghua University, Beijing, China

[6]Technical University Graz, Graz, Austria

Abstract

Numerous practical applications of the Discrete Element Method (DEM) require a flexible description of particles that can account for irregular and non-convex particle shape features. The importance of capturing particle non-convexity is that it allows for physical interlocking to be modeled when particles are in contact. To that end the most flexible approach to capture particle shape is by using a polyhedron which allows for a faceted representation of any shape albeit at significant computational cost. In this study we present a decomposition approach to model non-convex polyhedral particles as an extension to an existing open source convex polyhedral discrete element code, namely, BlazeDEM-GPU that computes using general purpose graphical processing units (GPGPUs). Although, the principle of convex decomposition of non-convex particles into convex particles is not new, it has received limited attention in the discrete element modeling community. This non-convex extension to BlazeDEM-GPU is validated against a hopper flow experiment designed using identical convex and identical non-convex 3D printed particles. In particular the experiment was designed around two sensitive flow points, such that the convex particles exhibit intermittent flow whereas the non-convex particles exhibit stable arches. The ability of the DEM simulations to reproduce both the convex and non-convex flow behavior using the same parameter set is demonstrated. This study is a significant step closer to general computing of non-convex particles for industrial scale applications using the GPGPUs.

1 Introduction

In nature and industrial processes, particles come as various shapes as depicted Figures 1(a) - (d). A key ingredient in a DEM simulation is the abstraction of complex particles into shapes suitable for computation. Abstractions include simple spheres, convex polyhedra, non-convex polyhedra and even non-convex large aspect ratio shapes often resulting in entangled media. Some two-dimensional abstractions are depicted in Figures 2 (a)-(d). Spherical particles can be representative of silica gel and ceramic granules in chemical processing to peas in the food industry, while salt and sugar crystals can be sufficiently approximated by convex polyhedral shaped particles. In turn, crystalline powders, crushed gravel and cement particles can be abstracted as non-convex polyhedra, while entangled media includes rigid staples and flexible woven fabrics as well as particles formed during granulation process.

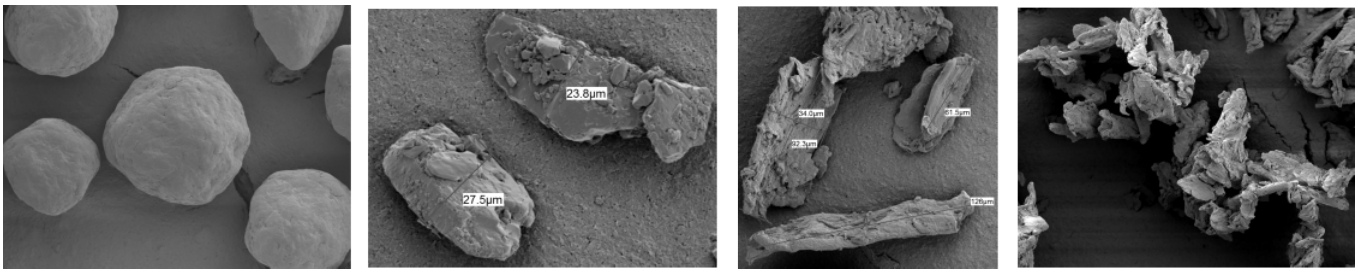

(a) (b) (c) (d)

Figure 1: Four examples of typical particles shapes for powders created by (a) spray-drying, (b, c) crystallization and (d) dry granulation that could be approximated by spherical, convex polyhedral, non-convex polyhedral and entangled non-convex polyhedral representations.

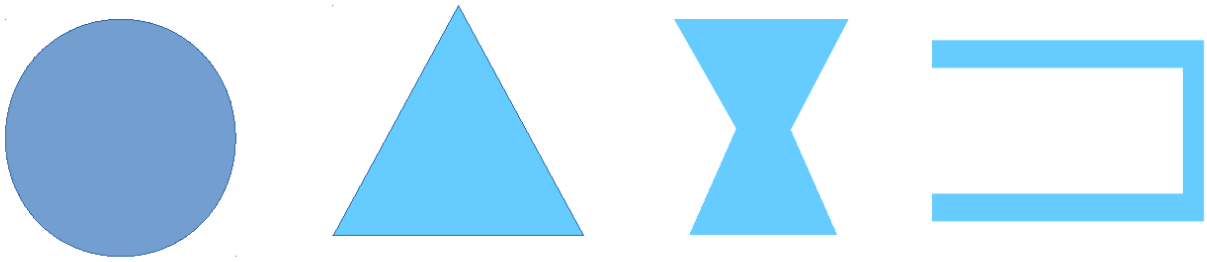

(a) (b) (c) (d)

Figure 2: Actual particle shapes abstracted as (a) spheroidal, (b) convex polyhedra, (c) non-convex polyhedra and (d) entangled non-convex polyhedra.

However, the geometrical abstraction of an actual particle is not the only consideration when DEM simulations are to be performed. Due to the computational demand to solve DEM, the computational cost of one abstraction over another plays a significant role in selecting a shape abstraction. In addition, simulation software may only offer

limited shape abstractions. In the DEM these have mainly been limited to spherical shaped particles or smoothed polyhedral shaped particles using spheres or cylinders to model geometric features. A prominent technique to model non-convex particles is the multi-sphere approach, which has the well known shortcoming that particle shapes lack angularity, an often critical particle property in many applications [1, 2, 3]. In addition, flat surfaces are approximated by spherical packing's resulting in artificial surface roughness effects.

Triangulation of particle surfaces aims to address some of the clumped-sphere shortcomings [4, 5]. However, both approaches place a significant computational burden on the computing resources, which in turn limits the number of particles that can be realistically computed. Consequently the number of large scale non-convex particle shaped simulations are limited. In fact, particle shape studies in general for large scale discrete element simulations have received little attention although the industrial importance thereof is well known [1, 2, 3]. Large scale industrial discrete element simulations can often only afford to abstract particle shapes as spheres or multi-spheres with few particles [2, 6, 7, 8].

An alternative is available to speedup computational times that may allow for more complex particle shape abstractions in large scale industrial simulations, which is to utilize graphical processing units (GPUs) to simulate the DEM. Recently, it has been demonstrated that convex polyhedral shape abstractions can be computed efficiently and for large scale industrial simulations on GPUs [9, 10, 11], a shape abstraction which used to be limited to CPU computing architectures [2, 12, 13, 14, 15, 16].

This study extends the shape abstraction for the GPU architecture to include non-convex particle shapes. This study builds on the limited non-convex or concave particle shape discrete element simulations that have been conducted on CPU architectures [5, 16, 17, 18, 19, 20, 21, 22]. Initial non-convex/concave particle shapes were limited to two dimensional abstractions that includes the work by Lim et al. Yang et al. and Alonso [18, 21, 23]. This was extended to three-dimensional smooth abstractions as demonstrated by Lim et al. [18], which requires non-uniform rational b-splines (NURBS) surfaces to represent the particles and a contact grid to resolve contact. Fleissner et al. [4] extended non-convex abstractions to include faceted bodies that can be in contact with spherical particles by conducting a surface triangulation of the faceted bodies. Smeets et al. [5] generalized this by considering non-convex abstractions of particles by applying a surface triangulation to non-convex particles which allowed them to simulate up to 3000 non-convex particles. Recently, Rakotonirina et al. [16] rekindled the well-known convex decomposition proposed by Chazelle [20, 24, 25], as a strategy to extend standard convex polyhedral contact resolution to resolve non-convex polyhedral contact using CPU architectures with MPI for 250 non-convex particles.

Following a convex decomposition approach, this study extends the convex polyhedral DEM code, BlazeDEM-GPU, to be able to handle non-convex polyhedral shaped particles on the GPU architecture. Our extension of BlazeDEM-GPU towards non-convex polyhedral shaped particles is validated against a carefully constructed experimental hopper discharge setup using monodispersed 3D printed particles. In addition, we demonstrate that we can compute with a million non-convex polyhedral shaped particles robustly and accurately within a realistic time frame due to the efficiency of our convex contact and decomposition implementation on the GPU.

1.1 Contact overview

In general, contact between convex polyhedra is first detected during a broad phase and resolved during a narrow phase. The broad phase estimates which particles are likely to be in contact by conducting a crude but computationally fast estimate. The contact pairs identified during the broad phase are then resolved during the narrow phase to compute the actual contact forces between particles. These forces are estimated in various ways, that include estimating the penetration distance [5, 26, 27], in vertex-face and edge-edge contact. Alternatively, contact can be resolved by computing the overlapping volume [5, 13, 28] from which the reaction forces are estimated.

1.2 Premise of this study

This study extends contact between convex polyhedra to contact between non-convex polyhedra following a decomposition approach. We construct a non-convex polyhedral particle from a number of convex polyhedral particles, which allows us to later decompose the non-convex particle into a number of convex particles. This multi-convex polyhedral approach is somewhat reminiscent of the multi-sphere approach that decomposes complex shapes into spherical particles. Following this choice, the broad phase contact detection and narrow phase detailed contact resolution is outlined in Figure 3. During the broad phase the non-convex particles that are likely to be in contact are identified as depicted in Figure 3(a). Contact between every identified non-convex particle contact pair is then refined using a secondary broad phase as outlined in Figure 3(b). In the secondary broad phase, the non-convex particles of an identified contact pair are decomposed into their respective convex constituents. This allows for contact detection between the convex constituents of particle 1 and particle 2 following a secondary broad phase in which the convex constituents that are potentially in contact are established. Contact is then resolved for the identified contact pairs between the convex constituents of particle 1 and particle 2 following a usual narrow phase contact resolution. In this study we note two decomposition strategies for the convex constituents that make-up a non-convex particle. A decomposition that has a zero or non-zero overlap amongst the convex constituents. This distinction has not been made before but is important to note as it affects the details of computing the inertia tensor, resolving the contact volume as well as potential implications towards particle breakage when considering breakage models that breaks a non-convex particle into its convex constituents. First, we outline the state of the art of our current convex polyhedra implementation in BlazeDEM-GPU by focusing our attention towards the narrow phase for convex polyhedral contact detection that accurately resolves the contact volume on the GPU.

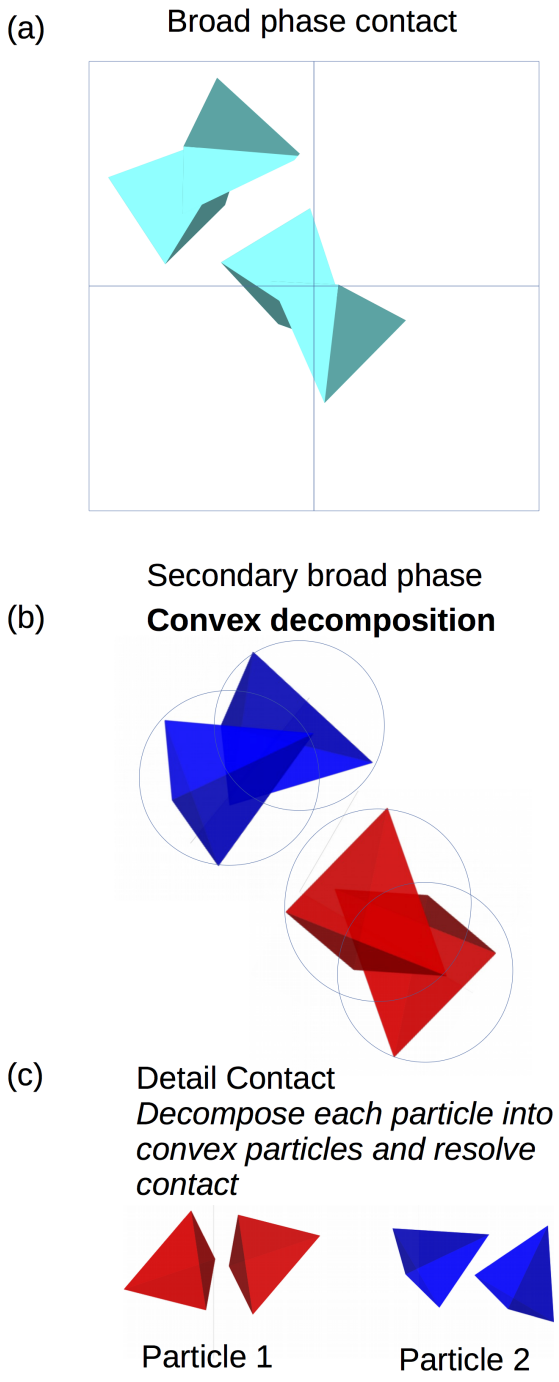

Figure 3: Non-convex polyhedral contact detection follows a (a) broad phase contact detection between two non-convex particles, followed by a (b) secondary broad phase contact detection between the individual convex constituents of particle 1 and particle 2. This is then followed by the (c) narrow phase in which the contact is resolved between all convex constituents of particle 1 and particle 2 that have been identified to be in potential contact.

2 Convex Polyhedra Representation

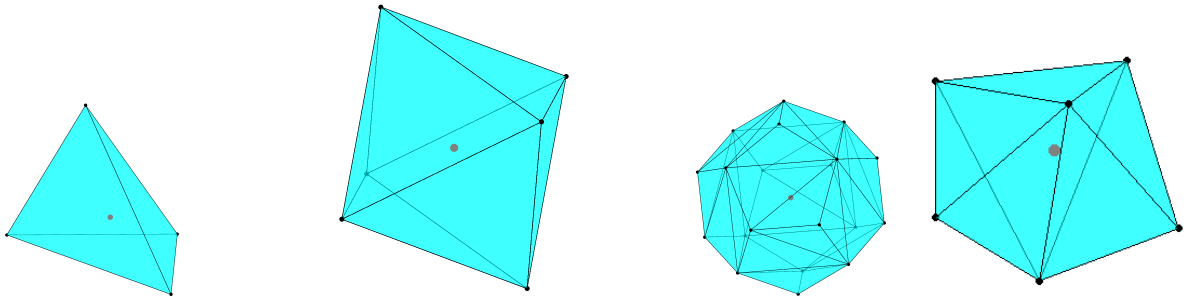

(a) (b) (c) (d)

Figure 4: Typical polyhedral shaped particles include (a) tetrahedron (b) octahedron and (c) dodecahedron and (d) pentagonal pyramid (Johnson solid J2 [29]). The centroids are indicated by red dots.

Recently, [30] demonstrated the possibility of employing a single level data structure by only storing the faces (or half spaces), i.e. for each face a point on the face and the face normal are stored, to define a convex domain that defines a convex particle as a set of linear inequalities. The overlap volume when two polyhedra are in contact is then defined by the combined set of linear inequalities between the two particles. Following linear programming terminology, the basic feasible solutions define the vertices of the overlap polyhedron. The convex hull of the vertices allows for the faces to be defined to ultimately resolve the reaction force magnitude and direction per particle. An alternative single level data structure could be achieved by storing only the vertices that define a convex hull, it would require the convex hull to be constructed on the fly every-time a particle is evaluated to allow for a surface integral to be performed to compute the reaction force magtinude and direction per particle. We circumvent the need for highly efficient particle representations by making use of a particle library to only store each particle type or template particle once in memory [9], each template particle is then orientated by a rotation and translation to an actual particle in the simulation. This minimalistic representation allows us to place data structures in the faster limited constant memory (48 KB) of the GPU [10].

Four typical polyhedral shaped particles are outlined in Figures 4(a) - 4(d). The rigid body mass parameters that include the mass m and inertia tensor $\mathbf{I}$ around the center of mass (COM) of the particles are required to compute the linear momentum

$$\mathbf{L} = m\mathbf{v}, \tag{1}$$

for a particle translating at velocity $\mathbf{v}$, and angular momentum

$$\mathbf{H} = \mathbf{I}\omega, \tag{2}$$

for a particle rotating with angular velocity ω. For a particle with volume V, the particle mass m given spatial mass density distribution $\rho(x, y, z)$ is obtained by integrating over the particle volume

$$m = \iiint_V \rho(x, y, z)dxdydz, \tag{3}$$

while the inertia tensor I_{ij} calculated at the COM is

$$I_{ij} = \iiint_V \rho(x, y, z)(r^2\delta_{ij} - r_i r_j)dxdydz, \tag{4}$$

with $r_i = (r_1, r_2, r_3) = (x, y, z)$, $r^2 = x^2 + y^2 + z^2$, δ_{ij} the Kronecker delta symbol with three indices $i = 1, 2, 3$ and $j = 1, 2, 3$ following the usual index notation convention. The inertia tensor I_{ij} calculated at the COM can be calculated relative to point $\mathbf{R} = R_1\mathbf{x} + R_2\mathbf{y} + R_3\mathbf{z}$, by the parallel axis theorem

$$J_{ij} = I_{ij} + m\left(|\mathbf{R}|^2\delta_{ij} - R_iR_j\right). \tag{5}$$

All these properties can be computed off-line for the various particle types employed in a simulation by following exact analytical integration or stochastic Monte Carlo integration. The approach we follow to compute these parameters for a convex polyhedral particle is as follows:

1. decompose a convex polyhedral particle into tetrahedra with zero overlap between them,
2. compute the volume, center of mass (COM) and inertia tensor of each tetrahedra using analytically derived expressions,
3. assemble the volume, center of mass and inertia tensor of the polyhedral particle from the tetrahedral contributions.

After the dynamic mass properties have been calculated we can conduct a dynamic simulation by explicitly integrating the change in linear and angular momentum to obtain the velocities and positions of each particle. Particles can interact between each other as well as the "world" geometry that confines them to a spatial domain. Two proportionality scaling for the contact force in three dimensions are typically used namely proportionality to

1. penetration distance [5, 31, 32, 33, 34, 20],
2. overlap volume [5, 13, 28].

The penetration distance (relative overlap) is by far the most popular contact modeling approach due to the computational efficiency thereof, in particular when polyhedral shaped particles are considered. However, when considering Figure 5(a) and (b) the same force is resolved when considering the penetration depth although in Figure 5(a) the entire side of the polygon has penetrated the other polygon as opposed to merely the corner as depicted in Figure 5(b). In addition, the reaction force directions are crudely approximated using the penetration depth as opposed to when computing the overlap volume as will become clear in the next section. The overlap volume that we implement results in an energy-conserving contact interaction scheme [35]. To the best of our knowledge the only two codes that resolve the overlap volume for convex polyhedra is the academic code BlazeDEM-GPU [10].

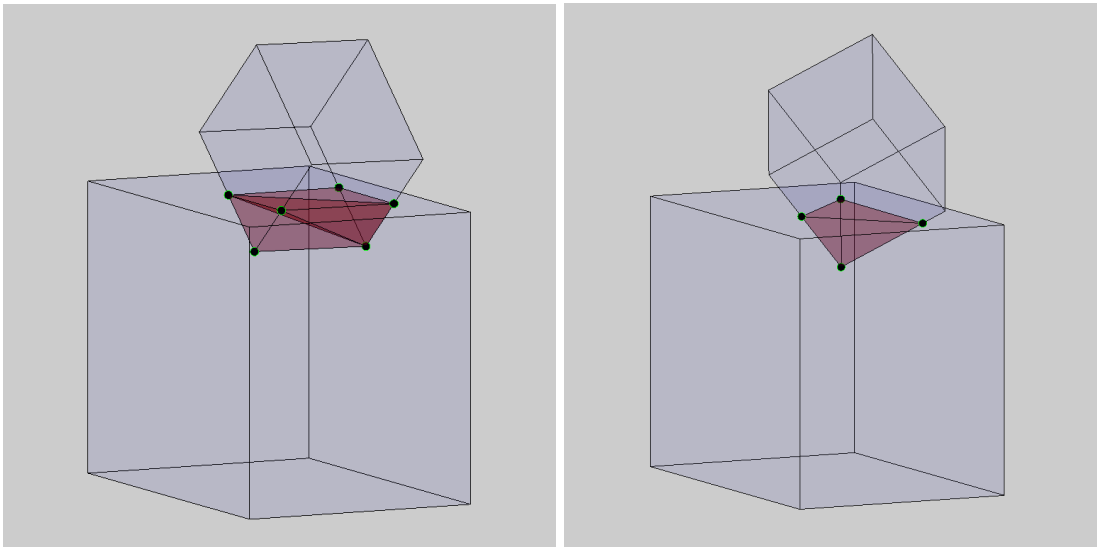

(a) (b)

Figure 5: Polyhedral contact with distinctly (a) larger and (b) smaller overlap volumes although the penetration depths are the same in both cases.

3 Non-convex Polyhedra Representation

In this study to model non-convex polyhedra we aim to reuse the algorithms developed to handle convex polyhedra as much as possible. This is made possible by following the convex decomposition of non-convex particles. The downside of this approach is that additional memory is required to store the information regarding each convex particle, while the benefits of a convex decomposition approach include:

1. basic modifications to the existing algorithms to include non-convex capability,
2. improvements made for convex polyhedral particle contact that will also benefit non-convex particle contact,
3. supporting functions to compute particle properties for convex particles can be reused for non-convex particles,
4. incorporation of simplified particle breakage model that breaks a non-convex particle into its convex constituents.

The broad phase can be resolved using two potential approaches, namely by

1. encapsulating the non-convex polyhedra into a bounding primitive object e.g. sphere or cylinder, or alternatively
2. identifying the separating planes for the convex hull representation of the non-convex particle.

In this study we consider the former approach of bounding primitives by applying the broad phase twice. First, the broad phase is applied for the entire non-convex particle. Should the possibility of contact between two particles have been established, we refine the broad phase by establishing which convex parts in each of the two particles are

potentially in contact by identifying the bounding primitives of the convex parts that are potentially in contact. Once, all potential convex-convex contact pairs in two contacting non-convex particles have been established we merely apply the narrow phase contact resolution between the convex-convex contact pairs to resolve in each case the overlap volume that ultimately defines the elastic force contribution for each convex-convex contact pair.

To enhance the flexibility of the convex decompositions of a non-convex particle we consider decompositions that have both non-zero and zero overlap (or intersection) between the convex particles that make-up a non-convex particle. The importance of this distinction is that following the decomposition approach with some overlap between the convex constituents, both the computation of particle properties such as the inertia tensor and the contact force of the overlap volume needs to account for the material that is accounted for multiple times between multiple convex particles. The contact force computation may circumvent this complexity should the contact of multiple overlap volumes be statistically unlikely, while particle properties can be computed for the non-convex particle as opposed to from the convex constituents. When there is no overlap between the convex particles it is evident that each convex decomposition uniquely represents material of the non-convex particle.

The percentage computational time spend in the detailed contact phase for hopper problems computed using convex polyhedra is typically around 80%. Evidently computing non-convex particles implies an additional burden on both the computer memory and computing resources. The need for additional memory resources is mitigated by the usage of a particle library. The worst case in terms of computational cost for non-convex to non-convex particle contact consists of n times m checks for a convex to convex contact, where n and m are the number of convex particles making up the two respective non-convex particles. Hence, given total computational cost C_C for a convex polyhedral hopper simulation, the worst case total non-convex compuational cost is estimated by $C_{NC} = 0.2C_C + 0.8C_C \times m \times n$.

3.1 Decomposition without any intersection between convex particles

Consider Figure 6(a) - (c) that depicts the tetrahedral decomposition of a non-convex polyhedron into three tetrahedra, with zero intersection between the polyhedra when assembled to form the non-convex polyhedron. In addition to simplifying the computation of the particle properties and resolution of the contact this approach may also benefit simplistic particle breakage models in which a particle breaks into its convex polyhedral constituents. The computation of the inertia tensor of the non-convex particle is merely the inertia tensors of the individual convex particles combined using the parallel axis theorem.

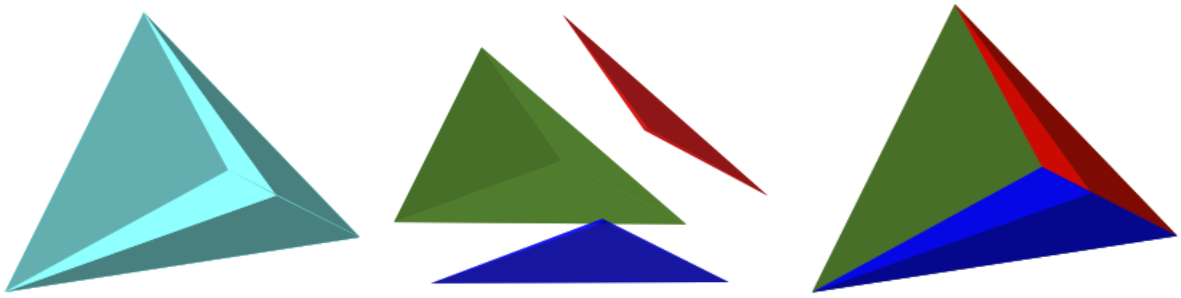

(a) (b) (c)

Figure 6: (a) Tetrahedron with one surface dented that is (b) decomposed into three tetrahedra and (c) assembled such that the intersection between the tetrahedra is zero.

3.2 Decomposition with significant intersection between convex particles

Consider Figure 7(a) - (c) that depicts the tetrahedral decomposition of a non-convex polyhedron into two tetrahedra, with non-zero intersection between the convex polyhedra when assembled to form the non-convex polyhedron. Here, the material associated with the overlapping volume between the two tetrahedra is duplicated. The computation of the inertia tensor of the non-convex particle is merely the inertia tensors of the individual convex particles combined using the parallel axis theorem with the inertia tensor of the overlap volume subtracted following the parallel axis theorem. Following this strategy of computing the overlap volumes between convex polyhedra we simplify the computation of particle properties such as the inertia tensor.

In addition, should the overlap volume between two contacting particles be duplicated between the non-zero intersect convex constituents we can compute the convex overlap domain and subtract it from the overlap volume, which can be computationally costly. For some non-convex particle compositions these contributions are negligible and can be ignored to speed-up the contact computation.

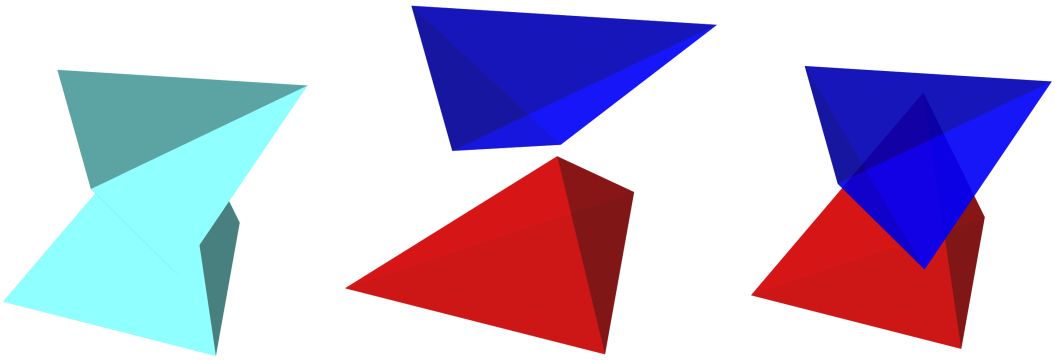

(a) (b) (c)

Figure 7: (a) Schönhardt polyhedron that is (b) decomposed into two tetrahedra and (c) assembled such that there is significant intersection between the tetrahedra.

4 Contact between Polyhedra

As stated contact between convex polyhedral particles is resolved by finding the overlap volume of two intersecting polyhedra. Although this is significantly harder than finding the overlap distance it does allow for both the direction and magnitude to be resolved following an energy-conserving contact interaction scheme [35]. We outline the steps involved in computing the overlap volume by considering the intersection of two polyhedral cubes as depicted in Figure 8(a).

Before we continue our discussion we note that the intersection volume between two intersecting polyhedra is convex and given by the convex hull formed using the vertices at the intersections between the polyhedral edges and surfaces [36]. The first step is to find the intersecting vertices as depicted in Figure 8(b), where after we define the surfaces that form the convex hull of the overlap volume as depicted in Figure 9(a). The surface normal $\mathbf{n}_i^{A_j}$ for each surface A_j of the convex hull is defined as depicted in Figure 9(b). Consider the contact volume in isolation as shown in Figure 10(a), it is clear that the surfaces of this volume is formed by the external surface of one polyhedra that is internal in the other polyhedra. We therefore need to identify which surfaces are internal to which body to ensure that we can compute the associated direction of the reaction force $\mathbf{n}_i^f$ on particle i. Once the surfaces have

been associated with a respective particle as shown in Figure 10(b), where each colour (red and green) is associated with a polyhedral particle, the resultant force can be computed by integrating over the surface normals over the contact area as shown by the black lines. The resultant force and surface normals associated with each particle is depicted in Figures 11(a) and (b) respectively.

Before we proceed two additional properties of the contact volume needs to be computed that will be required to resolve the elastic contact force namely, the contact Volume V and the center of mass (COM) of the contact volume. As both V and COM will change between contacts it is required to compute them efficiently on the GPU. The divergence theorem

$$\iiint_V (\nabla \cdot F)\, V = \oiint_{S(V)} F \cdot \mathbf{S}, \tag{6}$$

allows us to transform the volume integral of the object volume V into a surface integral with boundary surface $S(V)$. This can be done by appropriately choosing any vector field $\mathbf{F}(x_1, x_2, x_3)$ that has a divergence of 1 i.e. $\nabla \cdot \mathbf{F} = 1$. This then gives the volume

$$\oiint_{S(V)} F \cdot \mathbf{S} = \iiint_V V = V, \tag{7}$$

as a surface integral. Alternatively, the contact volume can be computed by breaking it into tetrahedra for which efficient closed form expressions exist in computing volumetric and inertial properties [37]. However, efficient inertial properties is not required as it can be computed off-line. In this study we compute the exact contact volume as opposed to approximating it [38]. Once, these quantities have been computed we can proceed to compute the direction of the reaction force

$$\mathbf{n}_i^f = \frac{\int_A \mathbf{n}_i^A ds}{|\int_A n_i^A ds|} = \frac{1}{\sum_j A^j} \sum_j A^j \mathbf{n}_i^{A_j}, \tag{8}$$

acting on particle i as shown respectively in Figures 11(a) and (b) for the two particles. Here, the direction of the reaction forces are respectively indicated by the dashed and solid black lines. In addition, the computed reaction force acts through the COM of the overlap volume, while the magnitude of the reaction force in turn is proportional to the volume V of the contact volume. The elastic force associated with contact volume, with volume V, for particle i follows the following constitutive relationship:

$$\mathbf{F}^i = kV\mathbf{n}_i^f, \tag{9}$$

where k is the volumetric stiffness with units Newton per meter cubed. In addition, the viscous damping force that depends on the relative velocity and rotation between the particles as well as the friction forces completes the contact forces on the particle [10, 9].

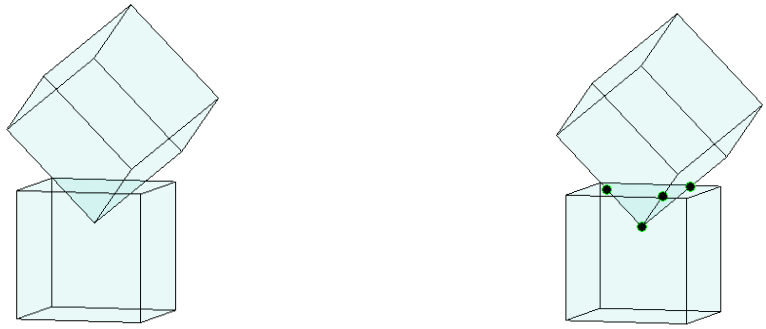

(a) (b)

Figure 8: (a) Two polyhedral cubes overlapping (b) intersection vertices are given as dots.

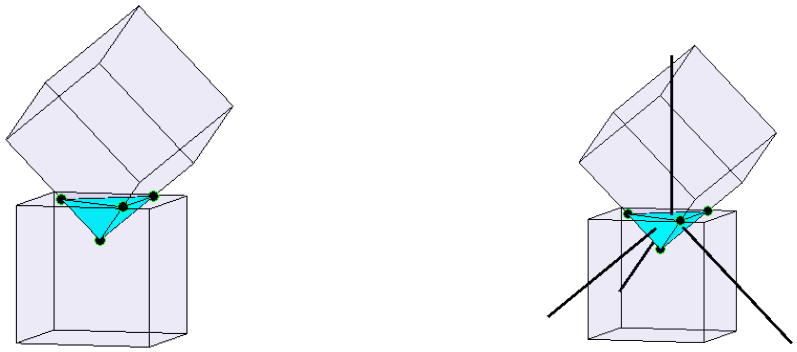

(a) (b)

Figure 9: Resulting (a) contact volume and (b) contact surfaces defined by the surface normals for two contacting polyhedral particles.

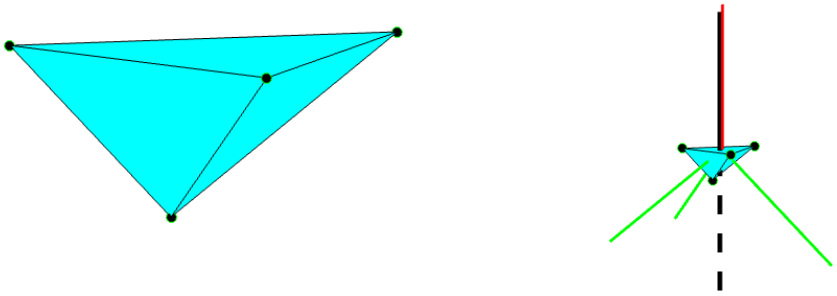

(a) (b)

Figure 10: (a) Isolated contact volume with (b) resulting force resultant (black lines) and surface normals associated with each particle given by the red and green lines.

(a) (b)

Figure 11: The decomposed the surfaces (defined by the surface normals) of the contact volume into surfaces internal to the (a) cube on bottom left and the (b) cube on the top right.

5 Validation

The convex triangular prism and non-convex Schönhardt polyhedral hopper discharge simulations are validated against an experimental hopper discharge using 3D printed monodispersed particles made from polylactic acid (PLA).

5.1 Experimental Setup

For this study we have selected the convex triangular prism and the non-convex Schönhardt polyhedron with great care as depicted in Figures 12(a) and (b). The convex triangular prism consists of two triangular faces and three rectangular faces. The Schönhardt polyhedron can be obtained from the triangular prism by rotating the two triangular faces of the prism by 45° relative to each other, after triangulating the three rectangular faces of the triangular prism. In particular, the rectangular faces are triangulated by a triangulation across the diagonal of the rectangle from bottom left to top right.

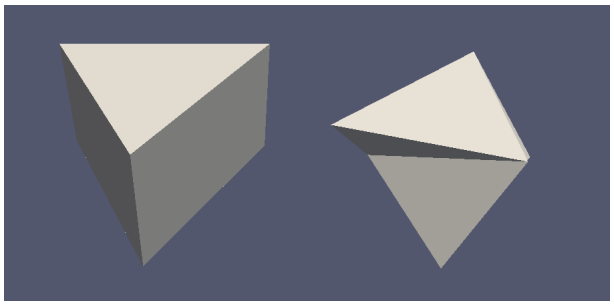

(a) (b)

Figure 12: Visual illustration of one triangular face of (a) a triangular prism and (b) a non-convex Schönhardt polyhedron obtained by rotating the two triangular faces of the triangular prism by 45° relative to each other. In addition, the three rectangular faces of the triangular prism are triangulated across the diagonal before rotation.

The two particles types were batch printed on a 9×17 grid of particles using four MBot Cube Duo 3D printers (Company: MBot, China) in the FabLab at IMT Lille Mines Douai. The overall geometric tolerance for the printed particles was within ± 0.1mm, effectively rendering a monodispersed particle setup [39]. Representative individual particles are depicted in Figure 13(a) and (b). The dimensions, print volume fraction (PVF) and average particle mass (APM) of the triangular prisms and Schönhardt polyhedra are given in Table 1. The particles were weighed and their densities adjusted to ensure all particles had the same weight to eliminate one of the controllable variances between the two particle types. This is done by adjusting the "Print Volume Fraction" (PVF) of each particle i.e. the percentage volume of material present when a unit volume is printed. This is achieved by printing the interior of a particle that is porous as opposed to solid, as shown in Table 1. One thousand black and one thousand white particles were printed of each particle type.

Table 1: Properties for the 3D printed particles.

Particle	Height (mm)	Side Length (mm)	PVF (%)	APM (g)
Triangular Prism	8.8±0.1	11.3±0.1	20	0.3469
Schönhardt Polyhedron	8.8±0.1	11.3±0.1	100	0.3470

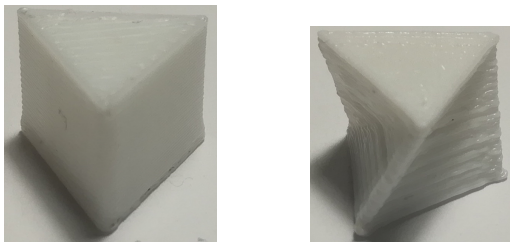

(a) (b)

Figure 13: Actual 3D printed (a) triangular prism and (b) Schönhardt polyhedron particle.

In this study the hopper discharge of both the convex triangular prism and non-convex Schönhardt polyhedron is investigated using a specifically designed hopper [11] as depicted in Figure 14 (b) with the dimensions as indicated in Figure 14 (a). The 4cm discharge opening was carefully selected after extensive experimental investigation to determine an appropriate discharge dimension that ensures the formation of stable arches for the Schönhardt polyhedron, while quasi-stable arches for particle systems of triangular prisms are observed to collapse. Quasi-stable here implies a temporary arch that is present for less than 2 seconds before is collapses, which implies 67% of the total discharge time of the experiment. For the triangular prism quasi-stable arches was observed from the start right towards the end of discharge. Although this was resolved with great care and effort, the advantage of carefully selecting this intermittent flow domain for the triangular prism and Schönhardt polyhedra is that it is sensitive i.e. slight changes result in either the absence of stable or quasi-stable arches. More importantly it also serves as an additional robustness check for the contact algorithm, as minor instabilities in the contact algorithm or integration scheme would result in the collapse of stable or quasi-stable arches.

The experimental hopper discharge of both convex triangular prism and non-convex Schönhardt polyhedral particles were conducted and representative discharges chosen to compare our numerical simulations against. Per simulation around 600 white particles and 400 black particles were used per discharge and packed in a layered fashion to allow us to better visualize the discharge. Due care was taken to isolate the setup from environmental vibrations, which is essential to capture stable arches and allow for higher repeatability in the experimental observations.

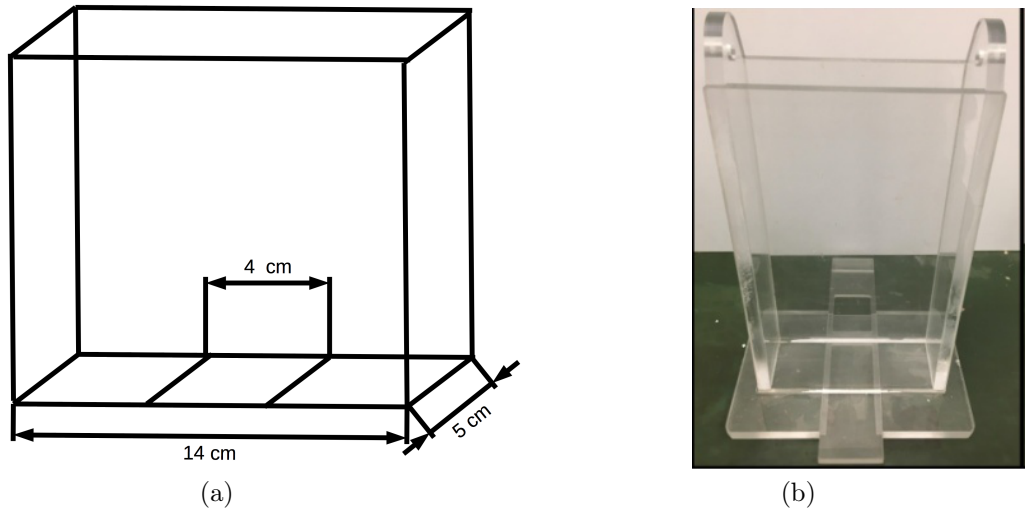

(a) (b)

Figure 14: Experimental hopper (a) dimensions and (b) constructed hopper made from plexiglass.

5.2 Simulation Setup

The geometry of the hopper is modeled as planes with dimensions as given in Figure 14(a) and stiffness listed in Table 2. During filling an additional plane is modeled over the opening, which is removed to model the discharge. The simulated triangular prism and Schönhardt polyhedra are depicted in Figures 15(a)-(b), with the (c) superimposed projects of the triangular prism (green vertices) and Schönhardt polyhedron (red vertices). In addition the vertices for each particle are listed in Table 2.

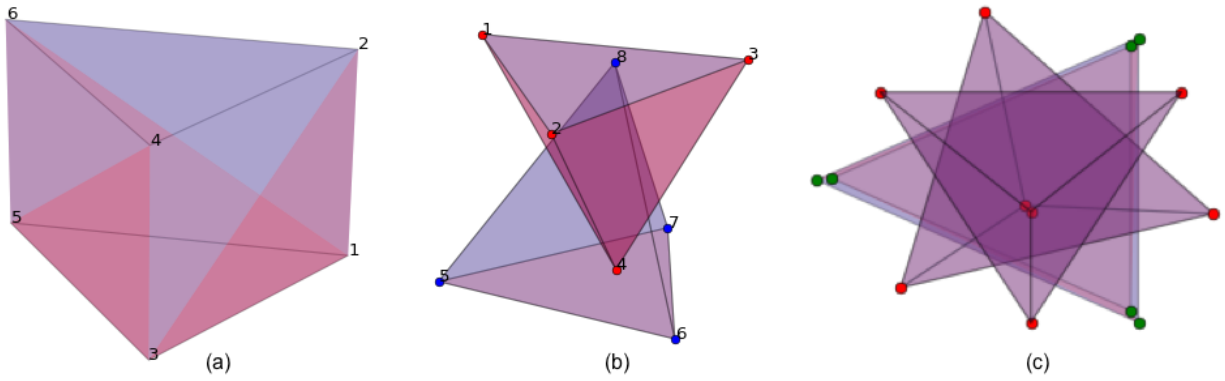

Figure 15: Simulated (a) triangular prism and (b) Schönhardt polyhedron, with the (c) superimposed projects of the triangular prism (green vertices) and Schönhardt polyhedron (red vertices). The particle vertices are listed in Table 2.

The DEM simulation parameters for the validation simulations are given in Table 3, which includes all particle specific parameters and general simulation parameters. A coefficient of restitution (COR) of 0.3 was used for the

Table 2: Vertices for the triangular prism and Schönhardt Polyhedron.

Vertex	Triangular Prism			Schönhardt Polyhedron		
Number	x (mm)	y (mm)	z (mm)	x (mm)	y (mm)	z(mm)
1	-3.67	-5.5	-4.40	-6.2	1.3	5.2
2	-3.67	-5.5	4.40	1.6	-6.5	5.2
3	-3.67	5.5	-4.40	4.4	4.1	5.2
4	-3.67	5.5	4.40	0.2	1.1	-3.6
5	7.33	0.0	-4.40	-5.5	-3.6	-3.6
6	7.33	0.0	4.40	5.5	-3.6	-3.6
7				0.0	6.0	-3.6
8				0.0	1.2	5.2

PLA printed particles which is within the 0.3 and 0.7 range for experimentally estimated COR [40]. The simulations were conducted on a single NVIDIA Titan X GPU.

Parameter	Symbol	Value	Unit
Triangular Prism Volume	V_{TP}	5.3240×10^{-7}	m^3
Schönhardt Polyhedron Volume	V_S	2.7044×10^{-7}	m^3
Triangular Prism Mass	m_{TP}	0.3469	g
Schönhardt Polyhedron Mass	m_S	0.3470	g
Triangular Prism Density	ρ_{TP}	652	kg/m^3
Schönhardt Polyhedron Density	ρ_S	1283	kg/m^3
Volumetric stiffness (PP)	k	98×10^9	N/cm^3
Volumetric stiffness (PW)	k	98×10^9	N/cm^3
Restitution coefficient (PP)		0.3	
Restitution coefficient (PW)		0.3	
Static friction (PP)		0.5	
Kinetic friction (PP)		0.4	
Static friction (PW)		0.7	
Kinetic friction (PW)		0.7	
Explicit integration time step	Δt	1×10^{-5}	s

Table 3: Simulation parameters for the triangular prism and Schönhardt polyhedron particle systems. (PP) indicates particle-particle and (PW) indicates particle-wall settings.

5.3 Hopper Discharge Results

The particles spaced on a regular grid of seven by two particles that then fell from a height of 20cm under gravity. The particles were iniitally placed with random orientation in the grid. In addition, the particles had random uniform initial horizontal velocities that ranged from 0 cm/s to 5 cm/s to simulate some of the variations of the experimental loading. The particle layers were colored post filling. The slight heaping to the right in the simulation is due to the stochastic nature of packing, each time obtaining a slightly different packing due to the random orientations. This results in a flow pattern and arch that is slightly skewed to the left. Averaged over 5 samples the pack height for the triangular prism was 124 (+/- 1) mm and 129 (+/- 1) mm for the Schönhardt polyhedra. Figure 16(a) and (d) depicts the hopper discharge of triangular prism and Schönhardt polyhedra at 0s, 0.8s, 1.6s and 2.4s respectively. Twenty experimental discharges were performed, with the depicted chosen as being representative

experimental discharges. It is evident that for the triangular prism quasi-stable arches form and are captured by Figure 16(a) 1.6s and and 2.4s. However, in most cases these arches eventually collapsed towards a discharged state of the hopper. In turn, stable arches formed almost in every case of the Schönhardt polyhedra, in particular after due care was taken to isolate the experimental setup from any environmental vibrations, as slight disturbances to the hopper resulted in additional discharge until the formation of the next stable arch. Figure 16(b) and (d) depict the simulated hopper discharges for the triangular prisms and Schönhardt polyhedra respectively. As can be seen qualitatively good agreement is achieved between the experiment and simulated discharges.

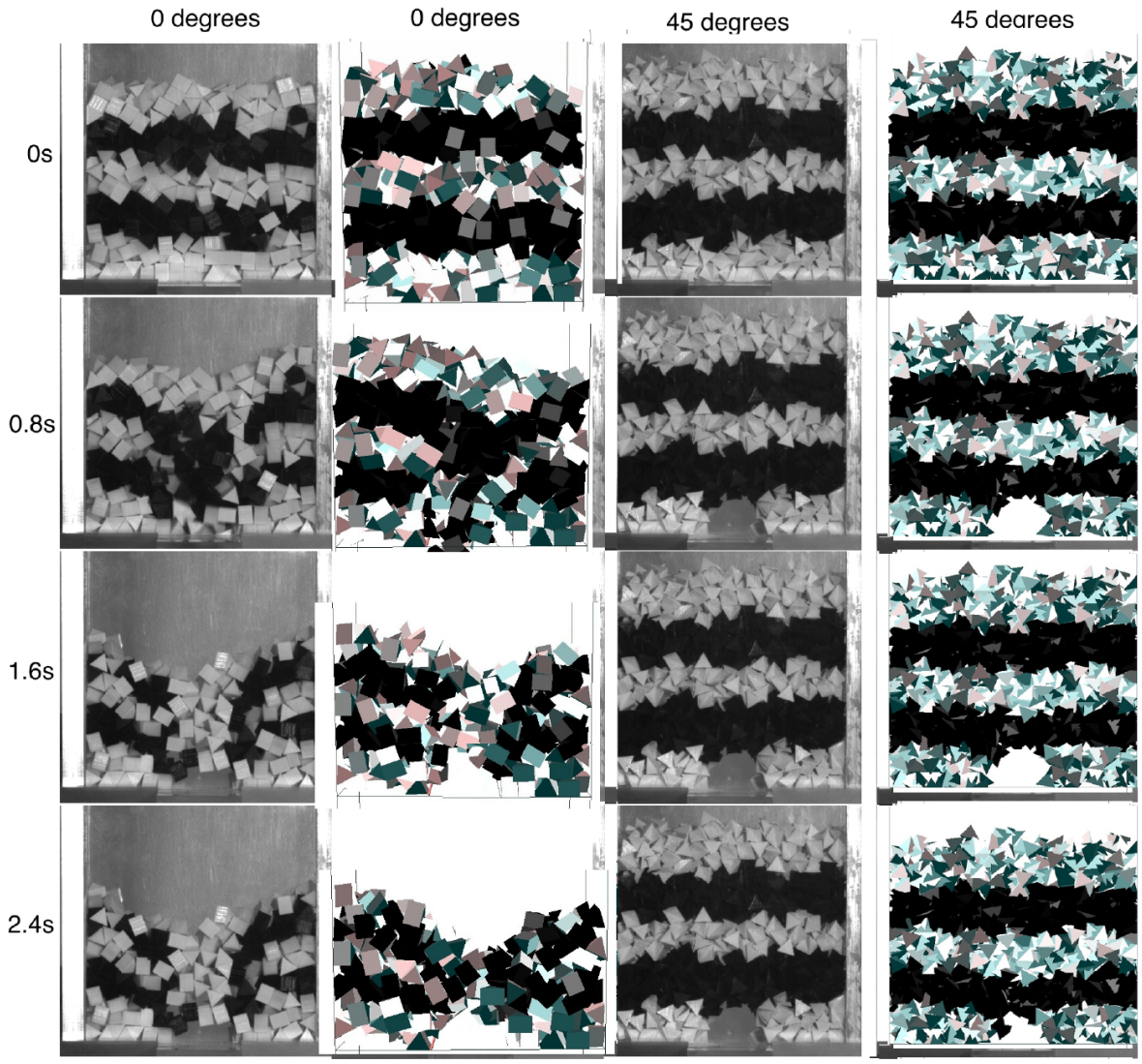

Figure 16: Validation for the (b),(d) simulated hopper discharge against the (a),(c) experimentally observed hopper discharge for the (a),(b) triangular prism) and (c), (d) Schönhardt polyhedra.

In addition, a quantitative comparison between the mass discharge for the convex triangular prism and non-convex Schönhardt polyhedron particle systems is depicted in Figure 17. Twenty experimental discharges were performed (indicated black dash lines) for each particle system with the simulated particle system indicated as a red solid line. It is evident that the experimental discharge is sensitive to the initial random packing of the particles, which is the only difference between the experimental runs. Random uniform initial horizontal velocities that ranged from 0 cm/s to 5 cm/s initial were introduced to simulate changes in the initial simulated packings that were deemed representative of the initial experimental packings. It is evident that the simulated discharge rates reflect the experimental discharge rates.

For the triangular prisms we observe a quasi-stable arch forming between 1.6s and 2.4s. Experimentally the quasi-stable arch formed between 1.6s and 2.4s, however experimentally quasi-stable arches were observed at numerous times as the flow for the triangular prisms is characterized by intermittent flow due to the formation of quasi-stable arches. For the Schönhardt polyhedra we observe a stable arch forming after 0.8s which coincided with our experimental observation. The initial shape of the arch coincides well with experimental observation. The arch remained stable over the duration of the simulation with the exception of deforming slightly over time, this is evident when looking at the shape of the arch at 0.8s, 1.6s and 2.4s. As the arch deformed over the 2.4 second simulation a total of ten particles discharged intermittently during the simulation without compromising the stability of the arch, whereas experimentally no additional particles were discharged and the arch not deforming over time as is evident from Figure 16(c). This is an important milestone in the simulation and prediction of stable arches in hopper discharge.

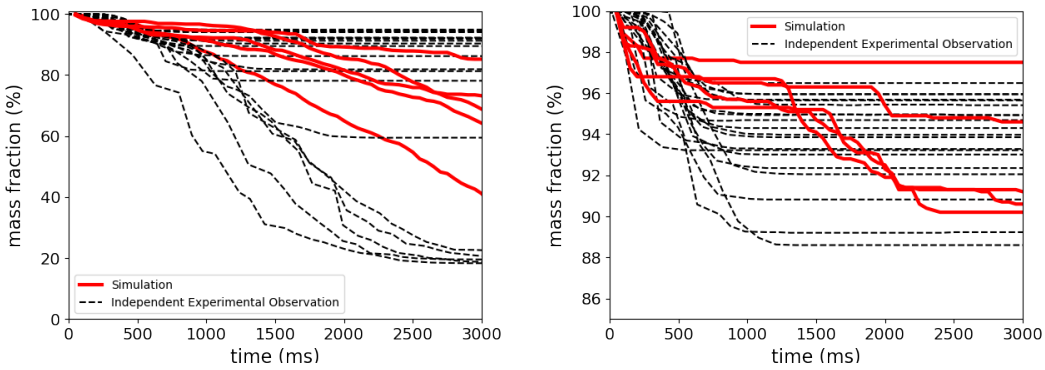

Figure 17: Twenty independent experimental discharge observations (dash black lines) and five simulated (solid red line) discharge for the (a) convex triangular prism and (b) non-convex Schönhardt polyhedron particle systems. Note that the range of the percentage mass fraction for figures (a) and (b) are different.

5.3.1 Velocity Field Comparison Between Convex and Non-convex (Non-Zero Intersection) Shaped Particles

In addition, to comparing the discharges we highlight the differences in the velocity field between the convex triangular prisms and non-convex Schönhardt polyhedra discharges when quasi-stable and stable arches form as depicted in Figures 18(a) and (b) respectively. The initial velocity field for the triangular prisms is developed over a larger domain than the highly localized velocity field for the Schönhardt polyhedra after 0.001s. After 0.8s a stable

arch has formed for the Schönhardt polyhedra that remains stable over the duration of the 2.4s simulation. In turn, a quasi-stable arch formed just after 0.8s for the triangular prism that destabilized around 1.3s.

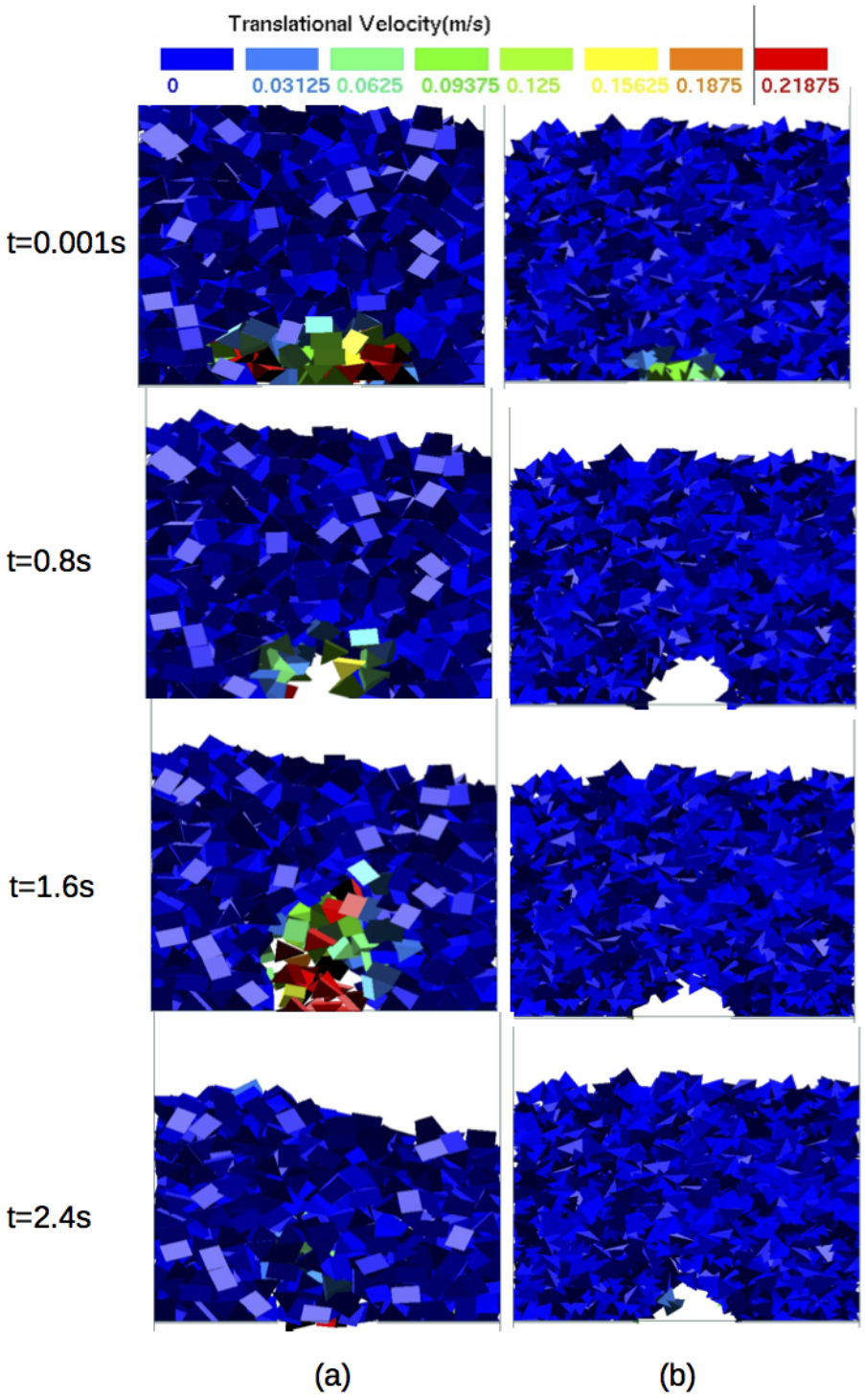

Figure 18: Comparison of the translational velocity magnitude between the (a) triangular prism and (b) Schönhardt particle systems at 0.001s, 0.8s, 1.6s and 2.4s.

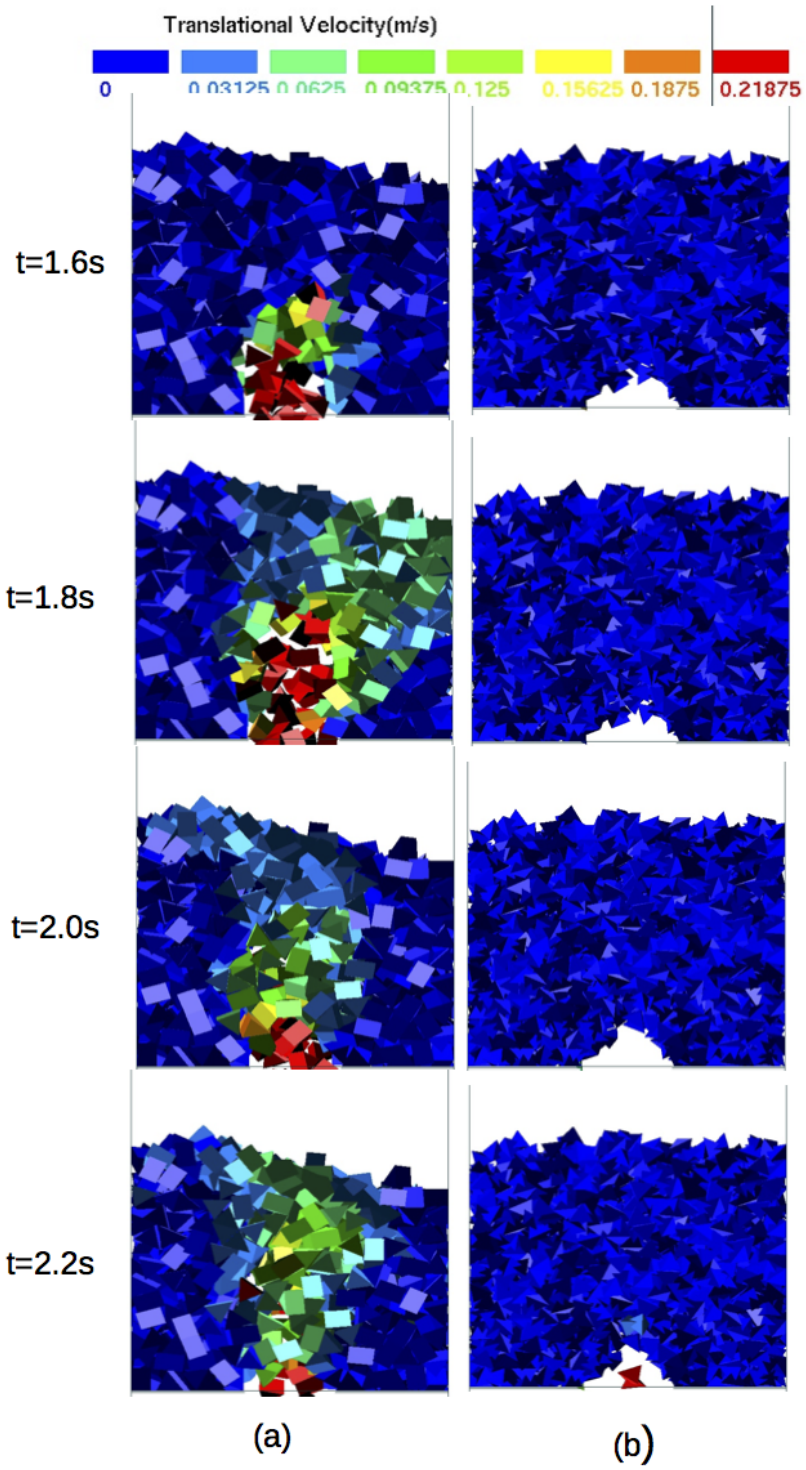

Figure 19: Comparison of the detailed translational velocity magnitude between the (a) triangular prism and (b) Schönhardt particle systems at 1.6s, 1.8s, 2.0s and 2.2s.

The development of the spatial flow field after 1.6s is well illustrated in Figures 19(a) and (b), in which we depict the velocity field after every 0.2s. The destabilization of the quasi-stable arch propagates towards the top right allowing for intermittent funnel flow to develop.

5.3.2 Force chains

Part of the complexity of granular media is the heterogeneous spatial distribution of inter-particle forces. The COM of two particles are linked by an edge or force chain when they are in physical contact with each other, while thickness of the force chain is determined by the force magnitude using a linear scale. A quantitative force comparison between the triangular prism and Schönhardt polyhedra, depicted in Figures 20(a)-(b) and Figures 20(c)-(d) respectively, reveals that the developed normal forces between the triangular prisms is up to three times higher and much more localized than the normal forces between the Schönhardt polyhedra. In addition, for the Schönhardt polyhedra the developed force chain network gradually increases with height with a well interlocked network of forces, while for the triangular prism the larger forces are not isolated to the bottom of the hopper. Consequently, the force chain network is more localized for the triangular prism network allowing for easier destabilization of the packing that ultimately results in a higher probability of flow of the particles. In turn the dense force chain network for the Schönhardt polyhedra with a lower spatial force chain magnitude variation allows for a more stable packing and a lower probability of flow of the particles. It is also evident for the stable arch that has formed at 2.0s for the Schönhardt polyhedra as compared to significant flow occurring at 2.0s for the triangular prism resulting in a disintegration of the lower force chain network.

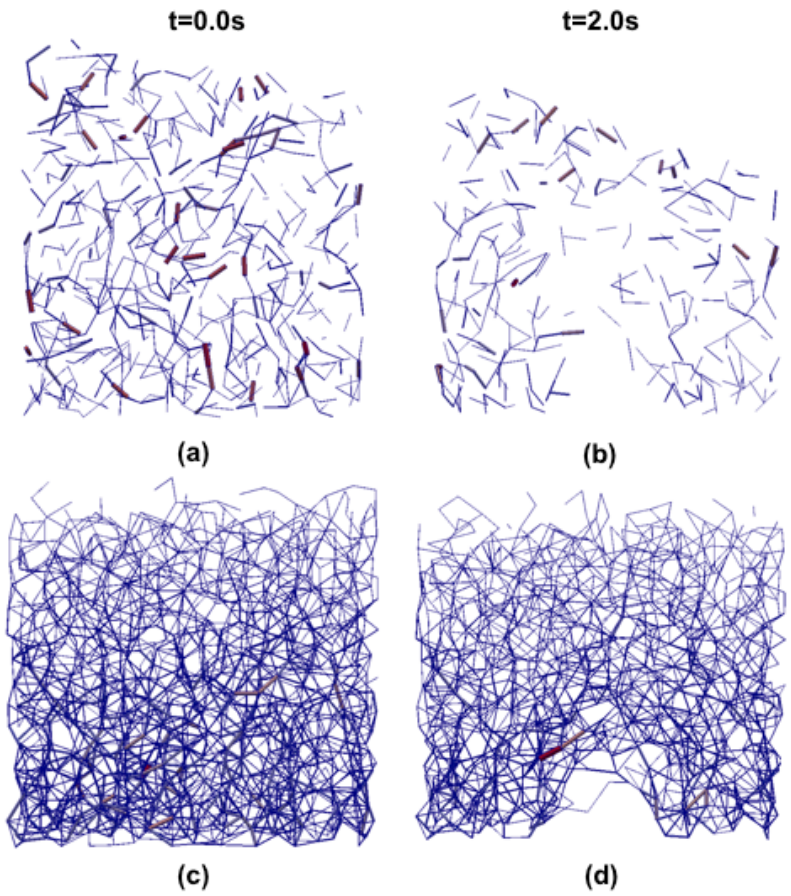

Figure 20: Developed force chains for the triangular prism at (a) 0.0s and (b) 2.0s, and for the Schönhardt polyhedra at (c) 0.0s and (d) 2.0s. The line thickness is proportional to the magnitude of the normal force.

5.4 Entangled Non-Convex Polyhedra

To further demonstrate the possibilites of the proposed contact method for non-convex particles and the numerical stability of our implementation we simulate entangled non-convex polyhedral particle systems by having two hollowed triangular prism (HTP) particles, as depicted in Figure 21(a), linked together. Each HTP is decomposed into nine convex particles. This is representative of entangled particle systems, where each particle is linked to another particle and free to translate and rotate relative to its linked particle within the constraints imposed by direct contact.

Although entangled media is prevalent in nature, from the meso [41, 42, 43, 44] to macro [45, 22, 46]length scales, limited studies have considered entangled non-convex polyhedra, Gravish et al. [22], due to the computational complexity and need for efficient robust contact detction algorithms to resolve the contact. Although, these particles are idealized and far from an industrially relevant shape they are easy to reproduce, adding to the scientific value as test problems, as well as playing an important role towards verifying the numerical robustness of the BlazeDEM-GPU framework.

For the simulations that follow 1024 hollow triangular prisms (HTP) and 1024 simplified dolos particles are respectively considered as depicted in Figure 21(a) and (e). Of the 1024 HTP particles, 64 are linked to form 32 linked hollow triangular prisms (majority of the particles are single particles). The solid volume and bounding radius for the HTP and simplified dolos particles are tabulated in Table 4, with the geometrical details of each particle depicted in Figures 21(a) and (e) respectively.

Shape	Solid Volume (m^{3})	Bound Radius (m)
Hollow Triangular Prism (HTP)	0.25×10^{-7}	0.98×10^{-3}
Simplified Dolos	0.27×10^{-7}	1.02×10^{-3}

Table 4: Details of the hollow triangular prisms (HTP) and simplified dolos particles.

The flow pattern states after 0s, 2.0s and 4.0s are depicted for the HTP particle system, while the simplified dolos particles that displayed significant locking are depicted for 0s, 2.0s and 8.0s. The respective mass fractions as a function of time are depicted in Figure 22 for the first three seconds of discharge. The simplified dolos particle system exhibit significant entangled locking, while the linked HTP particle system show intermittent interlocking.

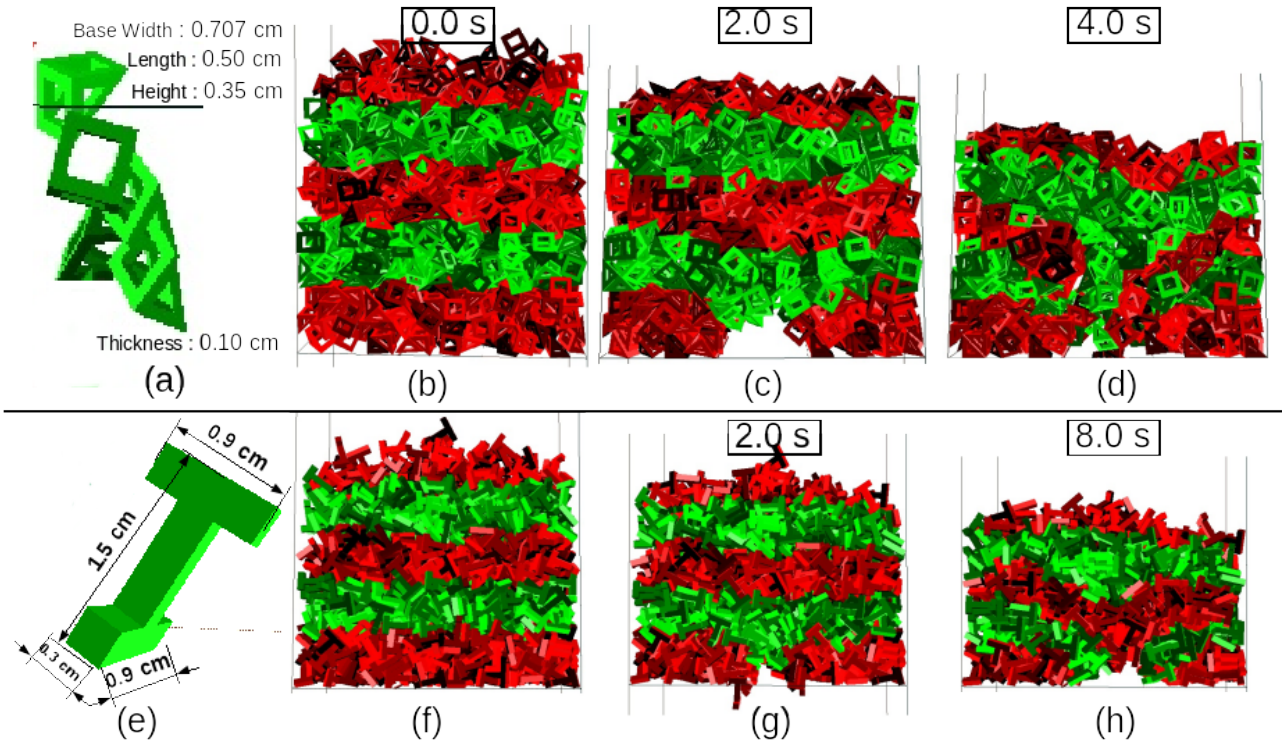

Figure 21: (a) Hollow triangular prism particles and flow patterns for (b)-(d) and (e) simplified dolos particle and flow patterns for (f)-(h).

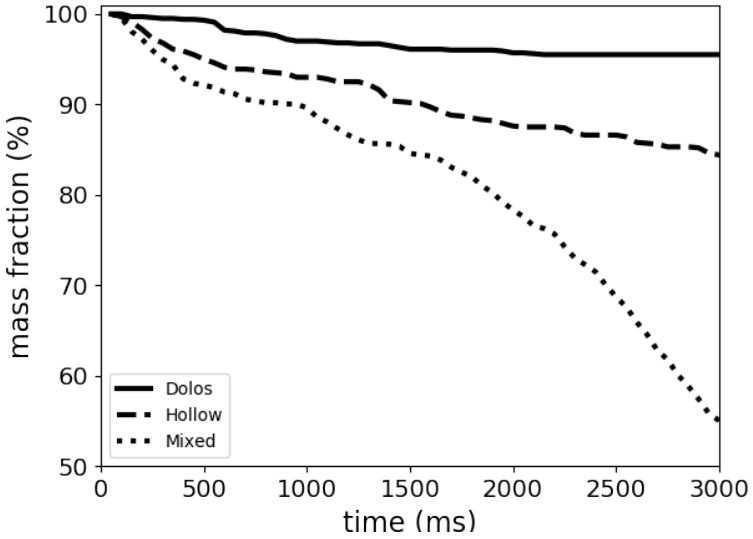

Figure 22: Mass fraction over time for the hollow triangular prism, simplified dolos and mixed particle systems.

Finally, we include a simulation with the mixture of the HTP and simplified dolos particle systems, scaled down to 25% of the sizes depicted in Figures 21(a) and (e), to illustrate the ability to handle non-uniform particle shape and particle size. A total of 2048 particles are considered consisting of 1024 hollow triangular prisms and 1024 simplified dolos particles. The initial particle distributions are uniformly mixed. The flow pattern states after 0s, 0.5s, 2.0s and 3.5s are depicted for the mixed particle system in Figure 23(a)-(e), respectively. The mass fraction for the mixed particle system is depicted in Figure 22, clearly indicating a much faster discharge towards the end than in the beginning. This highlights some of the more complex discharge behaviors of complex particle systems that exemplifies the need to accurately model particle shapes in particular when they introduce new interaction mechanisms such as physical interlocking and entanglement.

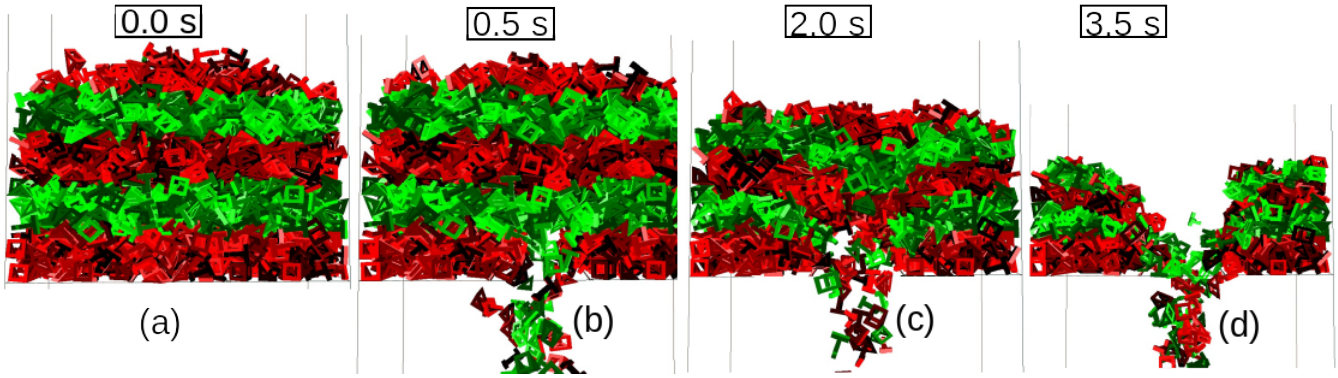

Figure 23: Flow pattern of the mixed particle system, existing of 1024 hollow triangular prisms and 1024 simplified dolos particles after (a) 0s, (b) 0.5s, (c) 2.0s and (d) 3.5s respectively.

Although these entangled particle illustrations are removed from industrially relevant particle shapes they do offer a valuable contribution towards investigating entangled particle systems as highlighted by the developed force chains depicted in Figures 24(a)-(c) for the linked HTP, dolos and mixed particle systems after 2.0s of discharge. It is evident that the developed force chain network for the dolos particle system is significantly more developed and balanced over the spatial domain than the linked HTP and mixed particle systems. The implication being that the force chain network is not so easily destabilized by small changes in a well developed force chain network as the force network offers multiple paths of support to particles over the hopper opening. In contrast the smaller particles of the mixed particle system after 2.0s is discharging freely as depicted in 23(c). The force chains link over smaller spatial distances as a result of particle size resulting finer detail in the force chain network. In addition, it is evident in 24(c) that the force chain network is the most developed around the edges of the hopper opening but offers limited support to the particles over the hopper opening resulting in discharge of particles. The force network of the linked TP, depicted in 24(a), offers partial support for particles over the hopper opening from the left edge, while the force network support for particles from the right edge is partially degraded.

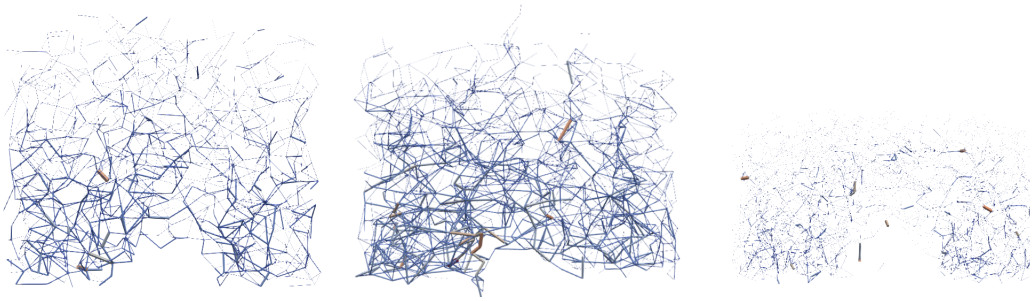

(a) (b) (c)

Figure 24: Developed force chains for the (a) linked hollow triangular prisms (b) dolos and (c) mixed particle systems after 2.0s of discharge.

6 Large scale simulation of Convex and Non-convex (Zero Intersection) Shaped Particles

We now consider the discharge of a convex tetrahedral particle system and non-convex dented tetrahedral particle system constructed from three tetrahedra without overlap as depicted in Figure 6. The dimensions of the convex tetrahedron and non-convex dented tetrahedron are identical except that one face of the dented tetrahedron is indented by one third of the height from the base to the apex. Each edge of the outer dimensions of the tetrahedron is 11.3 mm. In both simulations 262144 particles were used.

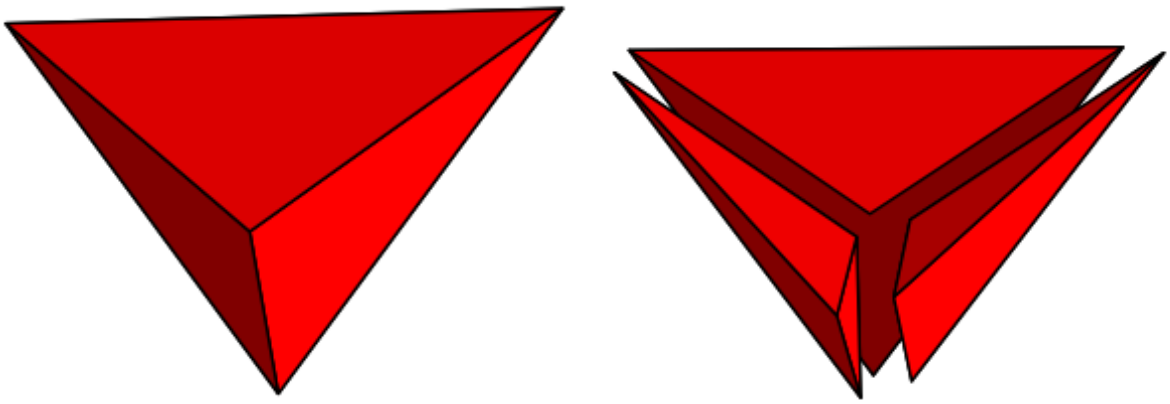

(a) (b)

Figure 25: (a) Tetrahedron and (b) disassembled dented tetrahedron, with edge lengths of 11.3mm, used in the large scale simulation.

The flow rates for the convex tetrahedral particle system and non-convex dented tetrahedral particle system are depicted in Figures 26 with the corresponding flow velocity fields and patterns in Figure 27. The mass fraction saturates at around 10%, as particles settle to the left and the right of the hopper basin. The two tetrahedra are identical with the only difference being that the dented tetrahedron has one surface dented inwards making it non-convex. The slower flow rate of the dented tetrahedron is evident in addition to a change in discharge slope around 300 ms. The importance of ,modeling non-convexity is again highlighted as it introduces a significantly different mechanism, namely physical interlocking, that may even be the dominating factor to model. This again highlights the importance of physical interlocking as a mechanism present in particle flow in addition to demonstrating that constructing non-convex particles from convex components with zero or non-zero intersection between the convex components is a viable and effective means to extend a convex polyhedral simulation platform.

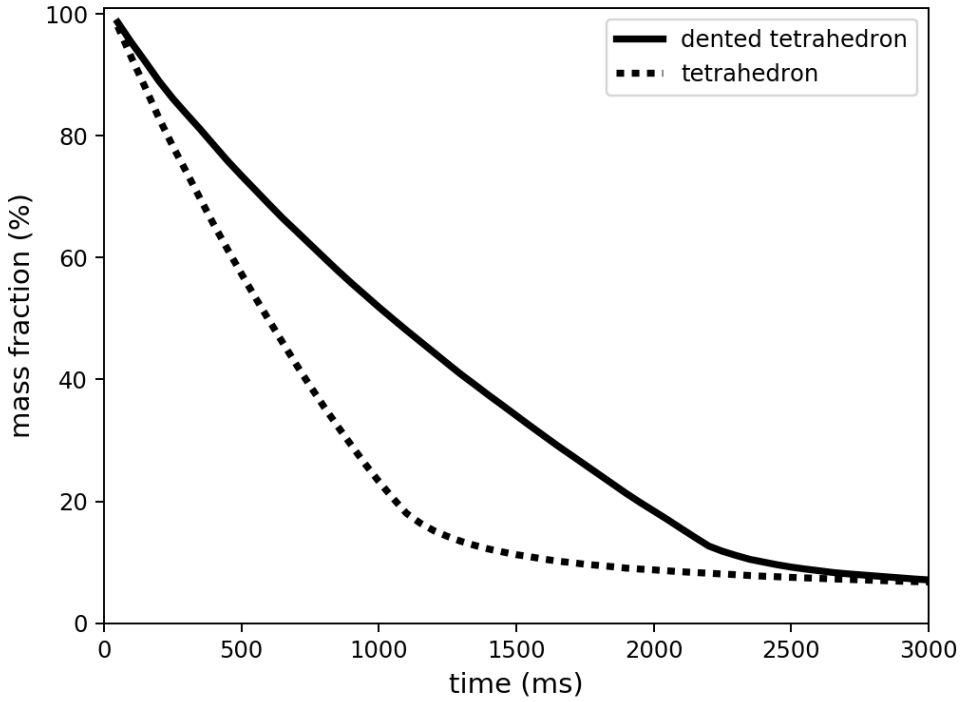

Figure 26: Mass fraction over time for the tetrahedron and dented tetrahedron particle systems.

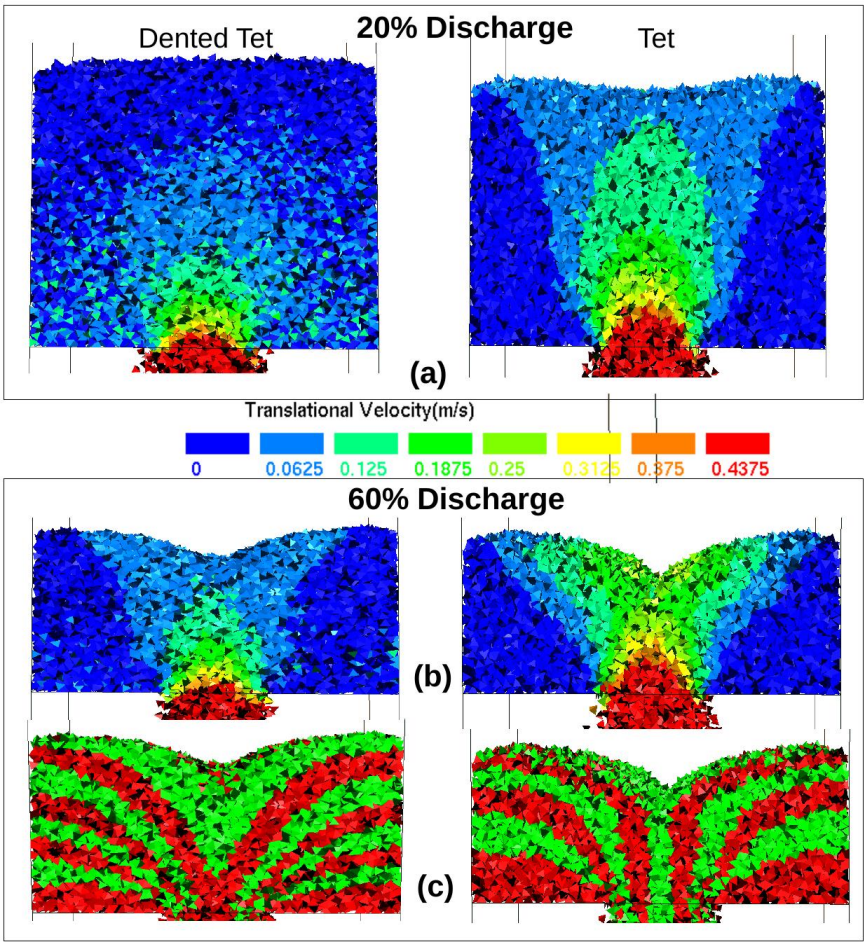

Figure 27: Flow velocity and pattern for the tetrahedron and dented tetrahedron particles after 20% and 60% of mass has discharged.

7 One Million Particle Drop Test

To conclude this study we consider a large scale packing to demonstrate the robustness of the convex and non-convex particle-particle and particle-wall contacts. The aim of the investigation is to ensure that the final number of particles after each simulation is indeed 1 million particles, in particular when subjected to this drop test where multiple impulse loads at various angles are imposed onto the particles. In addition, the drop test is conducted over a large surface area to allow for unstable particles to escape the packing should they go unstable. Although this mass balance test is rudimentary it remains an important test when polyhedral particles are considered to ensure robust and well resolved particle-particle contact, as stability can be challenging [47].

For this study in two separate simulations we packed 1 million convex triangular prisms and 1 million non-convex Schönhardt polyhedra in a 5m by 5m by 2m container. The initial particle velocities are 2 m/s and falling from a height of 1.75m. Each layer of particles consists of a regular grid of particles that is 4m by 4m and contains 26569

triangular prisms or 28561 Schönhardt polyhedra per layer.

The large scale packing depicted in Figures 28(a), (c) and (e) demonstrates robustness of the convex triangular prism particle-particle and particle-wall interactions, while the Figures 28(b), (d) and (f) demonstrate the non-convex Schönhardt polyhedra particle packing. The final number of particles in both simulations were 1 million particles i.e. no particles were lost over the course of the packing due to instabilities.

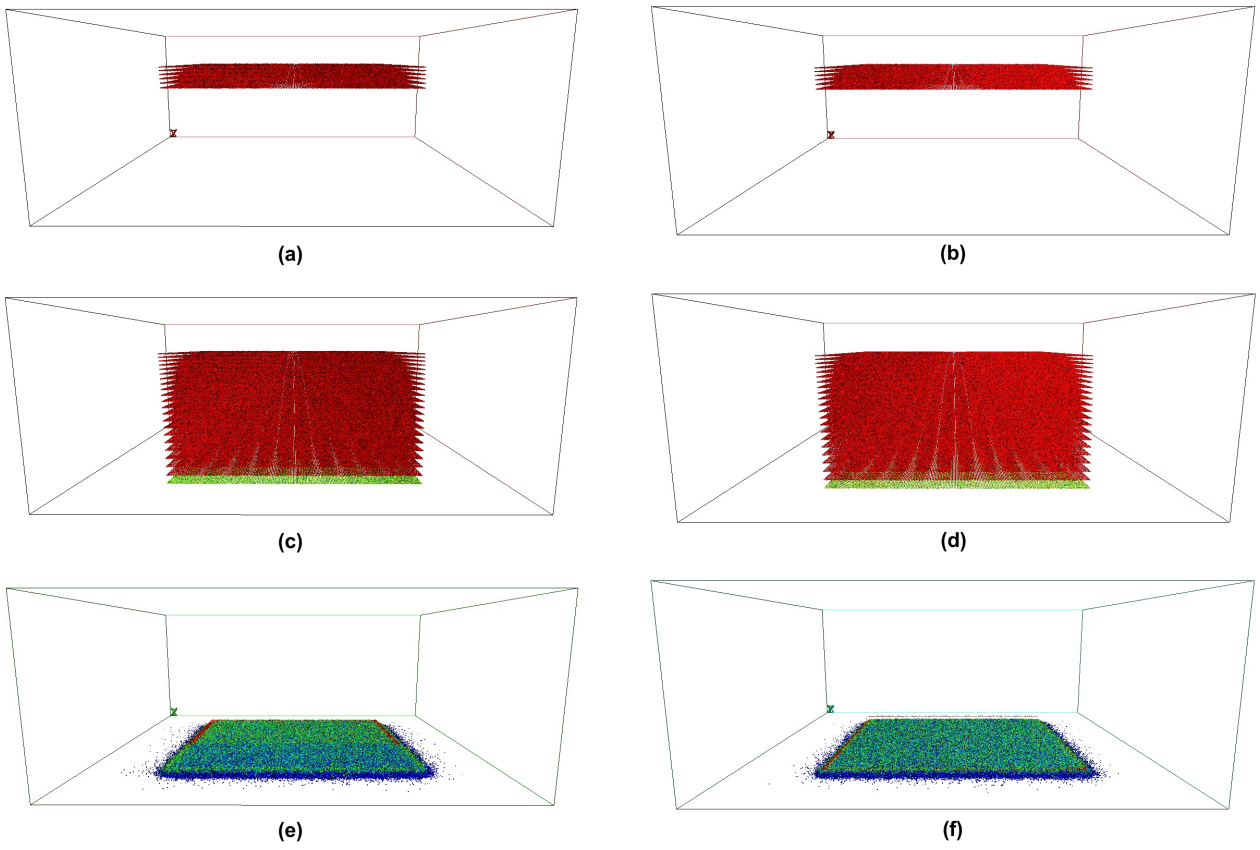

Figure 28: Packing of 10^6 convex triangular prism particles after (a) 0.1s, (c) first impact with floor (0.385s) and (e) impact of last layer (1.165s) and 10^6 non-convex Schönhardt polyhedral particles after (b) 0.1, (d) first impact with floor (0.385s) and (f) impact of last layer (1.100s).

8 Conclusions

This study demonstrated that non-convex particles can be efficiently modeled on a GPU computing architecture following a convex decomposition approach to model contact between non-convex particles. The benefit of this approach is that a significant portion of already developed convex contact machinery between polyhedral particles can be reused when available. The results were validated against a carefully constructed experimental study. In particular, the experiment was designed such that the convex particles exhibit quasi-stable arches, while the non-

convex particles exhibit stable arches. The ability of a discrete element simulation to capture fully stable arches is a significant validation test. The reason being that the explicit time integration inherently results in slight vibrations amongst the particles that may destabilize stable arches to exhibit quasi-stable arches or fully developed flow even when stable arch formation is expected. In addition, simulating stable arches serves as a significant test of the quality of the contact algorithms employed i.e. to be able to simulate stable arches the discrete element simulation needs to be devoid of any contact instabilities that would otherwise destabilize any arch formation. The stability of our contact algorithm was further stress tested by considering a 1 million particle drop test for both the convex and non-convex particle systems. The presented results that demonstrate that quasi-stable and stable arches can be simulated is a significant result and observation of this study. The difference in force chain networks between quasi-stable and stable arches were investigated, which clearly pointed to a dense network for the non-convex particle system in comparison to the convex particle system. This investigation pointed towards the benefit of simulation, allowing to visualize quantities not readily measurable experimentally. In addition, entangled non-convex particle systems are considered that demonstrates the potential for highly complex particle systems that exhibit significantly different hopper discharge behaviour. Lastly, as non-convex particles can become quite complex and difficult to reproduce by other researchers, we stress the importance of using reproducible particles by other researchers. In this study we utilized 3D printed particles to allow for a rigorous validation that allows for other researchers to reproduce the experimental findings. This is critical in moving DEM research forward [48], especially as the particle systems under investigation become more complex.

Acknowledgments

We gratefully acknowledge the support of the NVIDIA Corporation with the donation of the Titan X Pascal GPU used for this research, as well as the 3D printer equipment supplied by the FabLab des Mines de Douai. The financial support of the National Research Foundation (NRF) of South Africa is acknowledged.

References

[1] Paul W. Cleary. DEM prediction of industrial and geophysical particle flows. *Particuology*, 8(2):106–118, 2010.

[2] G. Lu, J.R. Third, and C.R. Müller. Discrete element models for non-spherical particle systems: From theoretical developments to applications. *Chemical Engineering Science*, 127:425–465, 2015.

[3] C R K Windows-Yule, D R Tunuguntla, and D J Parker. Numerical modelling of granular flows: a reality check. *Computational Particle Mechanics*, 3(3):311–332, 2016.

[4] F. Fleissner, T. Gaugele, and P. Eberhard. Applications of the discrete element method in mechanical engineering. *Multibody System Dynamics*, 18(81), 2007.

[5] B. Smeets, T. Odenthal, S. Vanmaercke, and H. Ramon. Polygon-based contact description for modeling arbitrary polyhedra in the Discrete Element Method. *Computer Methods in Applied Mechanics and Engineering*, 290:277–289, 2015.

[6] E. Rougier, A. Munjiza, and J.P. Latham. Shape selection menu for grand scale discontinua systems. *Engineering Computations*, 21(2/3/4):343–359, 2004.

[7] H. Kruggel-Emden, S. Rickelt, S. Wirtz, and V. Scherer. A study on the validity of the multi-sphere Discrete Element Method. *Powder Technology*, 188(2):153–165, 2008.

[8] Chong Shi, De-jie Li, Wei-ya Xu, and Rubin Wang. Discrete element cluster modeling of complex mesoscopic particles for use with the particle flow code method. *Granular Matter*, 17(3):377–387, 2015.

[9] Nicolin Govender, Daniel N. Wilke, Schalk Kok, and Rosanne Els. Development of a convex polyhedral discrete element simulation framework for NVIDIA Kepler based GPUs. *Journal of Computational and Applied Mathematics*, 270:386–400, 2014.

[10] Nicolin Govender, Daniel N. Wilke, and Schalk Kok. Collision detection of convex polyhedra on the NVIDIA GPU architecture for the discrete element method. *Applied Mathematics and Computation*, 267:810–829, 2015.

[11] Nicolin Govender, Daniel N. Wilke, Patrick Pizette, and Nor-Edine Abriak. A study of shape non-uniformity and poly-dispersity in hopper discharge of spherical and polyhedral particle systems using the Blaze-DEM GPU code. *Applied Mathematics and Computation*, 319:318–336, 2018.

[12] E.G. Nezami, Y.M.A. Hashash, Dawei Zhao, and Jamshid Ghaboussi. A fast contact detection algorithm for 3-D discrete element method. *Computers and Geotechnics*, 31(7):575–587, 2004.

[13] C.W. Boon, G.T. Houlsby, and S. Utili. A new algorithm for contact detection between convex polygonal and polyhedral particles in the discrete element method. *Computers and Geotechnics*, 44:73–82, 2012.

[14] M.A. Hopkins. Polyhedra faster than spheres? *Engineering Computations*, 31(3):567–583, 2014.

[15] Alexander Podlozhnyuk, Stefan Pirker, and Christoph Kloss. Efficient implementation of superquadric particles in Discrete Element Method within an open-source framework. *Computational Particle Mechanics*, 4(1):101–118, 2017.

[16] Andriarimina Daniel Rakotonirina, Jean-yves Delenne, and Anthony Wachs. A parallel Discrete Element Method to model collisions between non-convex particles. In *Powders & Grains: EPJ Web of Conferences*, volume 140, pages 1–4, 2017.

[17] Hans-Georg Matuttis and Jian Chen. *Understanding the Discrete Element Method: Simulation of Non-Spherical Particles for Granular and Multibody Systems*. Wiley, 2014.

[18] Keng-wit Lim, Kristian Krabbenhoft, and José E Andrade. On the contact treatment of non-convex particles in the granular element method. *Computational Particle Mechanics*, 1(3):257–275, 2014.

[19] John R Williams and Ruaidhr O Connor. Discrete Element Simulation and The Contact Problem. *Archives of Computational Methods in Engineering*, 6(4):279–304, 1999.

[20] Ben Nye, Anton V Kulchitsky, and Jerome B Johnson. Intersecting dilated convex polyhedra method for modeling complex particles in discrete element method. *International journal for numerical and analytical methods in geomechanics*, 38(May):978–990, 2014.

[21] Y Yang, J F Wang, and Y M Cheng. Quantified evaluation of particle shape effects from micro-to-macro scales for non-convex grains. *Particuology*, 25(Supplement C):23–35, 2016.

[22] Nick Gravish and Daniel Goldman. Entangled granular media. In Alberto Fernandez Nieves and Antonio Manuel Puertas, editors, *Fluids, Colloids and Soft Materials: An Introduction to Soft Matter Physics*, pages 341–354. Wiley, first edition, 2016.

[23] F Alonso-Marroquín. Spheropolygons: A new method to simulate conservative and dissipative interactions between 2D complex-shaped rigid bodies. *EPL (Europhysics Letters)*, 83(1):14001, 2008.

[24] Bernard Chazelle. Convex Decompositions of Polyhedra. In *Proceedings of Thirteenth Annual ACM Symposium on Theory of Computing (STOC)*, pages 70–79, Milwaukee, 1981.

[25] Chanderjit L Bajaj and Tamal K Dey. Convex Decomposition of Polyhedra and Robustness. *SIAM Journal on Computing*, 21(2):339–364, 1992.

[26] Victor Klee. Maximal Separation Theorems for Convex Sets. *Transactions of the American Mathematical Society*, 134(1):133–147, 1968.

[27] Helge Tverberg. A separation property of plane convex sets. *Mathematica Scandinavica*, 45(2):255–260, 1980.

[28] Jan Elias. DEM simulation of railway ballast using polyhedral elemental shapes. In *III International Conference on Particle-based Methods Fundamentals and Applications*, pages 1–10, 2013.

[29] Norman W. Johnson. Discrete Element Simulation and The Contact Problem. *Canadian Journal of Mathematics*, 18:169–200, 1966.

[30] C.W. Boon, G.T. Houlsby, and S. Utili. A new rock slicing method based on linear programming. *Computers and Geotechnics*, 65:12–29, 2015.

[31] S Cameron and R Culley. Determining the minimum translational distance between two convex polyhedra. In *IEEE International Conference on Robotics and Automation*, pages 591–596, 1986.

[32] E. G. Gilbert, D. W. Johnson, and S. S. Keerthi. A fast procedure for computing the distance between complex objects in three-dimensional space. *IEEE Journal on Robotics and Automation*, 4(2):193–203, 1988.

[33] P.K Agarwal, L.J Guibas, S Har-Peled, A Rabinovitch, and M Sharir. Penetration depth of two convex polytopes in 3D. *Nordic Journal of Computing*, 7(3):227–240, 2000.

[34] S.J Lee. *Developments in large scale discrete element simulations with polyhedral particles*. PhD thesis, University of Illinois at Urbana-Champaign, 2014.

[35] Y T Feng, K Han, and D R J Owen. Energy-conserving contact interaction models for arbitrarily shaped discrete elements. *Computer Methods in Applied Mechanics and Engineering*, 205-208:169–177, 2012.

[36] D.E. Muller and F.P. Preparata. Finding the intersection of two convex polyhedra. *Theoretical Computer Science*, 7(2):217–236, 1978.

[37] F Tonon. Explicit Exact Formulas for the 3-D Tetrahedron Inertia Tensor in Terms of its Vertex Coordinates. *Journal of Mathematics and Statistics*, 1(1):8–11, 2004.

[38] Jyh-Ming Lien and Nancy M Amato. Approximate Convex Decomposition of Polygons. In *Proceedings of the Twentieth Annual Symposium on Computational Geometry*, SCG '04, pages 17–26, New York, NY, USA, 2004.

[39] A.V. Potapov and C.S. Campbell. Computer simulation of hopper flow. *Physics of Fluids*, 8(11):2884–2894, 1996.

[40] Kamran Kardel. *An analytical and experimental study on 3D-printed custom surfaces for benthic algal biofilms*. PhD thesis, Auburn University, 2016.

[41] Philipse AP. The random contact equation and its implications for (colloidal) rods in packings, suspensions, and anisotropic powders. *Langmuir*, 12(5):1127–1133, 1996.

[42] Brown E, Zhang H, Forman NA, Maynor BW, Betts DE, DeSimone JM, and Jaeger HM. Shear thickening and jamming in densely packed suspensions of different particle shapes. *Physical Review E*, 84:031408, 2011.

[43] Manna L, Milliron DJ, Meisel A, Scher EC, and Alivisatos AP. Controlled growth of tetrapod-branched inorganic nanocrystals. *Nature Materials*, 2(6):382–385, 2003.

[44] Chen S, Wang ZL, Ballato J, Foulger SH, and Carroll DL. Monopod, bipod, tripod, and tetrapod gold nanocrystals. *American Chemical Society*, 125(52):16186–16187, 2003.

[45] Gravish N, Franklin SV, Hu DL, and Goldman DI. Entangled granular media. *Physical Review Letters*, 108(20):208001, 2012.

[46] A. Menges. *Material synthesis : fusing the physical and the computational*, volume 85 of *AD Architectural Design*. Wiley, 2015.

[47] U Rüde. Massively Parallel Non-Smooth Granular Dynamics and its Coupling with Lattice-Boltzmann Methods. In *V International Conference on Particle-based Methods: Fundamentals and Applications*, pages 1–2, 2017.

[48] Daniel N. Wilke, Patrick Pizette, N Govender, and N.-E. Abriak. Towards reproducible experimental studies for non-convex polyhedral shaped particles. In EDP Sciences, editor, *EPJ Web of Conferences*, page 06028, 2017.